# Nano-scale simultaneous observation of Li-concentration profile and Ti-, O electronic structure changes in an all-solid-state Li-ion battery by spatially-resolved electron energy-loss spectroscopy

CrossMark

Kazuo Yamamoto [a,*], Ryuji Yoshida [a], Takeshi Sato [a], Hiroaki Matsumoto [b], Hisanori Kurobe [a], Tadashi Hamanaka [a], Takehisa Kato [c], Yasutoshi Iriyama [c], Tsukasa Hirayama [a]

[a] Nanostructures Research Laboratory, Japan Fine Ceramics Center, 2-4-1 Mutsuno, Atsuta-ku, Nagoya, Aichi 456-8587, Japan
[b] Global Application Center, Hitachi High-Technologies Corporation, 11-1 Ishikawa-cho, Hitachinaka, Ibaraki 312-0057, Japan
[c] Department of Materials, Physics and Energy Engineering, Nagoya University, Furo-cho, Chikusa-ku, Nagoya, Aichi 464-8601, Japan

## HIGHLIGHTS

- SR-TEM-EELS visualizes the Li profile and changes of Ti and O electronic structure.
- Titanium and oxygen contribute to the charge compensation of the inserted Li.
- Picometer-scale expansion of the O—O distance due to the Li insertion is visualized.
- *In-situ*-formed negative electrode inserted by Li has an amorphous structure.
- Amorphous-electrode/solid-electrolyte interface reduces the interfacial resistance.

## ARTICLE INFO

## ABSTRACT

All-solid-state Li-ion batteries having incombustible solid electrolytes are expected to be promising candidates for safe next-generation energy storage devices that have a long lifetime and high energy density. However, it is essential to address the large resistance of Li-ion transfer at the electrode/solid-electrolyte interfaces. A new concept electrode that is formed *in situ* from the $Li_2O$—$Al_2O_3$—$TiO_2$—$P_2O_5$-based glass-ceramic solid electrolytes with Si and Ge doping (LASGTP) produces atomic scale connection at the interfaces, which provides extremely low interfacial resistance. However, the formation mechanism and the reason for the low resistance are still unclear. Here we applied spatially-resolved electron energy-loss spectroscopy in a transmission electron microscope mode (SR-TEM-EELS) to visualize the nanometer-scale Li distribution and its effects on the electronic structures of other important elements (Ti and O). Local electron diffraction showed that the *in situ* formed electrode was an amorphous phase caused by the Li insertion. Picometer-scale expansion of O—O distance due to the Li insertion was also visualized in the electrode. These electronic and crystal changes and gradual Li distribution contribute to the low resistance and stable battery cycles.

© 2014 Elsevier B.V. All rights reserved.

## 1. Introduction

Lithium-ion batteries (LIBs) [1] are essential for numerous uses in business, industry, and daily life. However, conventional LIBs with flammable liquid electrolytes have some problems in terms of safety, reliability, lifetime, cost, and energy density. All-solid-state LIBs with incombustible solid electrolytes have enormous potential to overcome such problems [2]. However, the large interfacial resistance of Li-ion transfer at the electrode/solid-electrolyte interfaces prevents their practical use. Extensive efforts have been made to reduce the resistance at these interfaces [3—6]. One effective solution is an *in situ* formation of active electrode materials from the parent solid electrolytes [3,7—9]. Because the electrodes grow from the solid electrolytes, both materials probably become connected to each other at an atomic scale, leading to low

interfacial resistance. Such electrodes were discovered in $Li_2O-Al_2O_3-TiO_2-P_2O_5$-based glass–ceramic solid electrolytes [8,9] (LATP, manufactured by OHARA Inc., Japan [10]). A negative electrode was formed *in situ* near the negative-side LATP/current–collector interface by decomposition with an excess Li-insertion reaction. The interfacial resistance was measured to be at most 100 $\Omega cm^2$, which was much lower than that at a conventional deposited-electrode/solid-electrolyte interface, for example, 4000 $\Omega cm^2$ at the $LiCoO_2$/LATP interface [11].

Electron holography (EH) was recently applied to visualize the local electric-potential distribution in a transmission electron microscope (TEM) [12], and the fabrication process of the *in-situ*-formed negative electrodes was dynamically observed during the battery reaction [11,13]. The electric potential gradually decreased in a 700-nm-wide region near the negative-side LATP during the charging process. However, EH can detect only local electric-potential change; thus, the structural growth mechanism is still unclear, as is the cause of the low interfacial resistance, the electronic structures of the negative electrodes, and the relationship between the local potential change and the Li concentration.

Here, we used spatially-resolved electron energy-loss spectroscopy in TEM mode (SR-TEM-EELS) [14,15] to directly visualize the nanometer-scale Li-concentration profiles around the *in-situ*-formed-negative-electrode/solid-electrolyte interface. The SR-TEM-EELS technique can also be applied to detect the precise electronic changes of other important elements, for example Ti and O included in the LATP, as chemical shifts of the EEL spectra. Some experimental reports have indicated that the transition metal (such as Ti) and O elements play significant roles when the Li-ions are inserted into some battery materials [16,17]. Those elements would contribute to the *in situ* formation of the negative electrodes and the redox reaction of the battery cycles. In this paper, we show the SR-TEM-EELS images of Li, Ti, and O around the *in-situ*-formed-negative-electrode/solid-electrolyte interface. Nano-scale simultaneous analysis of the images revealed not only a nanometer-scale Li profile but also a significant relationship of the above three elements in the Li insertion/extraction reaction: $Ti^{3+}/Ti^{4+}$ electronic changes, the influence on Ti/O electronic hybridization orbits, picometer-scale expansion of O–O distances by Li insertion, and the relation with the electric potential observed by EH.

## 2. Experimental

### 2.1. Preparation of the all-solid-state LIB for TEM observation

Fig. 1(a) illustrates the all-solid-state LIB sample we prepared for this study. A Si- and Ge-doped LATP sheet (LASGTP, 90 μm thick, by OHARA Inc.) was used as the solid electrolyte. The crystalline phases in the LASGTP glass matrix are composed of $Li_{1+x}Al_xGe_yTi_{2-x-y}P_3O_{12}$ (main-phase), $Li_{1+x+3z}Al_x(Ge,Ti)_{2-x}(Si_zPO_4)_3$ (sub-phase), and $AlPO_4$ [18]. The former two phases are sodium (Na) super ionic conductor (NASICON)-type structures. The 800-nm-thick film of the $LiCoO_2$ positive electrode was deposited at 873 K for 10 h on one side of the sheet by pulsed laser deposition (PLD), and then the gold (Au) was coated using a sputtering method onto the $LiCoO_2$ as the current collector. On the negative side, the platinum (Pt)-current-collector was directly deposited on the other side of the LASGTP. Small copper (Cu) plates were electrically connected on the current collectors using a silver paste, and then cyclic voltammetry (CV) was carried out for 50 cycles in a vacuum with a sweep rate of 40 mV min$^{-1}$. During the CV, the Li ions extracted from the $LiCoO_2$ charge around the LASGTP/Pt interface, which causes the irreversible formation of the *in-situ*-formed negative electrodes. Fig. 1(b) plots the CV curves at the 1st, 10th, and 50th cycles. Because the largest amount of Li
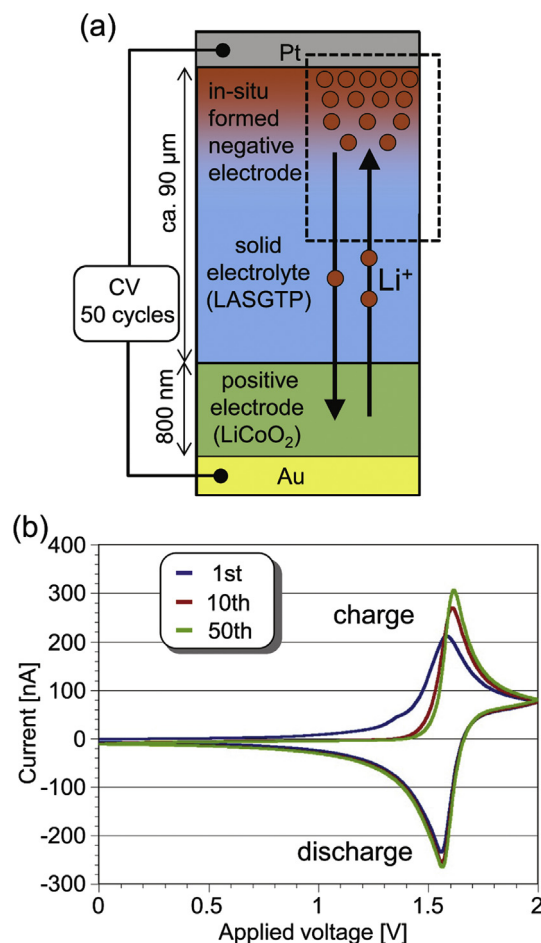


Fig. 1. All-solid-state LIB sample and its cyclic voltammogram. (a) Illustration of the prepared all-solid-state LIB cell. (b) Cyclic voltammogram (CV) measured in a vacuum with a sweep rate of 40 mV min$^{-1}$.

insertion/extraction occurs at 3.93 V (vs. Li/Li$^+$) in the $LiCoO_2$ [19] and at 2.35 V (vs. Li/Li$^+$) in the negative electrode [8], the charge and discharge current peaks are clearly seen around the applied voltage of 1.6 V. This means that the Li-inserted region worked stably as the negative electrode even after 50 CV cycles. After the CV cycles, a small piece was lifted out from the negative side of the LIB sample by using a micro-sampling method in a focused ion beam (FIB) system (Hitachi, FB2100), and was thinned to a thickness of about 100 nm for TEM observation. To transfer the TEM sample from the FIB system to the TEM or an Ar glove box, the sample was put into an Ar environment covered by a glove bag in order to avoid air exposure.

### 2.2. Experimental set-up of SR-TEM-EELS

An experimental set-up of the SR-TEM-EELS system is shown in Fig. 2(a). The parallel electron beams are uniformly illuminated to the sample. Thus we can observe the TEM image at the bottom of the TEM column. A region of interest in the TEM image is selected with a rectangular slit on the front of the EELS system, and the energy-loss electrons resulting from inelastic scattering due to the battery sample are dispersed by a magnetic prism. The two-dimensional energy-dispersed plane is magnified by some lenses installed in the EELS system, and the plane is recorded by a charge-coupled-device (CCD) camera. A typical spectrum image is illustrated in Fig. 2(b). The horizontal and vertical axes correspond to
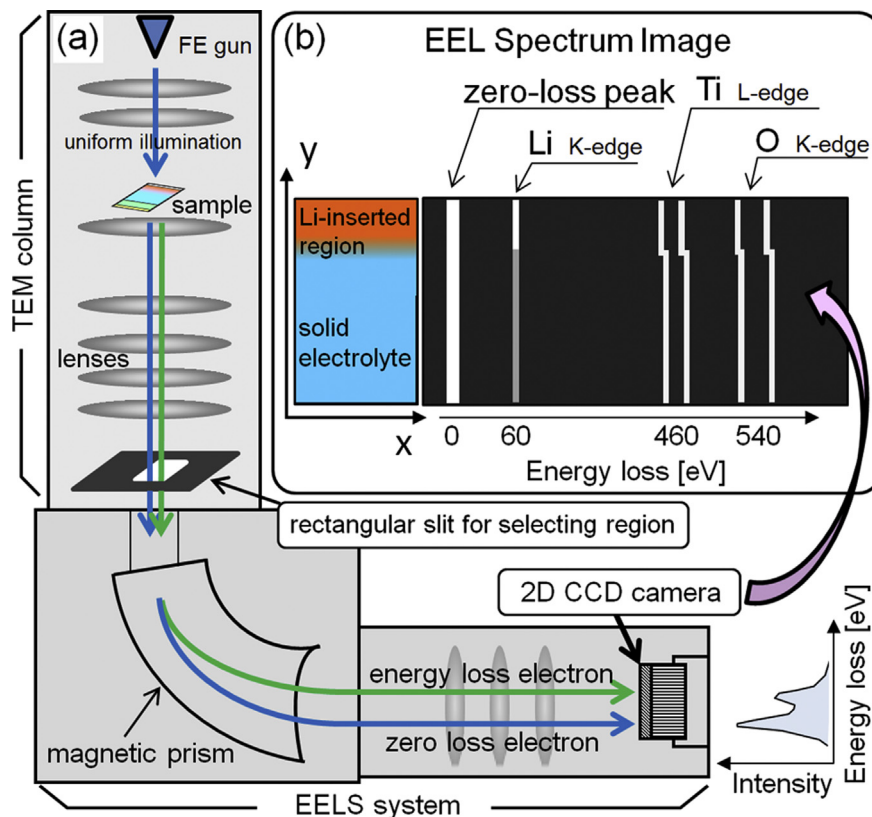
**Fig. 2.** Experimental setup of SR-TEM-EELS. (a) Ray diagram of zero-loss electrons and energy-loss electrons in the TEM column and EELS system. A region of interest is selected by the rectangular slit, and then the energy-dispersed plane is recorded by a 2D CCD camera. (b) Illustrative spectrum image obtained by SR-TEM-EELS. The horizontal and vertical axes indicate the electron energy-loss and the position of the sample, respectively.

the energy-loss of incident electrons and the sample position along the $y$-direction. The spectrum signals along the $x$-direction of the sample are integrated in the spectrum image. Thus, the rectangular slit needs to be set perpendicular to the sample layers. When the selected region includes Li, Ti, and O elements, the corresponding main EELS peaks appear as white lines along the vertical axis around the energy-losses of 60, 460, and 540 eV, respectively. If there is a difference in the Li concentration, we can see a change in the intensity of the Li white line. The remarkable advantages of this technique are that it enables not only elemental profiling but also high precision measurement of chemical shifts of the EEL spectra that result from changes in the electronic structure, for example $Ti^{4+}$ to $Ti^{3+}$ by Li-insertion. Although the common EELS measurement using a scanning transmission electron microscope (STEM) provides 2D spectra, the positions of the zero-loss peaks (ZLPs) sometimes change because of the disturbance of external electromagnetic fields, mechanical vibration, and electron beam tilt during the beam scanning, which deteriorates the reliability of the chemical shifts of the spectra. In SR-TEM-EELS, however, the spectrum image illustrated in Fig. 2(b) is recorded simultaneously with uniform illumination of the electron beam. Therefore, even if the energy drifts of the ZLPs are generated during the acquisition, the whole spectrum image drifts by the same value, and as a result, the chemical shifts of spectra (for example Ti or O in Fig. 2(b)) are maintained in the region. The precision of the chemical-shift analysis is determined by the distortion of the white line of the ZLP. We carefully adjusted the lenses of the EELS system so that the ZLP line would be straight along the $y$-direction, and the distortion was less than 0.1 eV (see the ZLP line in Supplementary data 1). We used a 300-kV TEM (Hitachi, HF3300) equipped with an EELS

system (Gatan, GIF Quantum ER) for the SR-TEM-EELS measurement. The spectrum images were taken by using a CCD camera ($2048 \times 2048$ pixels) under the condition of 0.1 eV/pixel.

## 3. Results and discussion

### 3.1. Crystal structure changes of the in-situ-formed negative electrode

Fig. 3(a) shows the TEM image around the negative side. In the LASGTP solid electrolyte region, we observed black, gray, and white contrast regions, which respectively represent the above three phases [18] from the elemental maps shown in Fig. 4. However, a slightly uniform contrast layer (about 400 nm) was observed near the Pt current-collector (Fig. 3(a)). This layer was the region of the *in-situ*-formed negative electrode where the Li ions were inserted as described later (Figs. 5 and 6). The electron diffraction patterns from the layer (Fig. 3(b)) and the parent LASGTP substrate (Fig. 3(c)) are the evidence that the Li insertion caused the above two NASICON-type crystals to change to the amorphous phase because no diffraction spots are observed in Fig. 3(b). This kind of connection between the amorphous electrode and the solid electrolyte seems to have a lot of paths of Li-ion transfer, indicating low interfacial resistance.

Some cracks were observed in the negative electrode region as indicated by the arrows in the enlarged image of Fig. 3(d). The grains near the cracks correspond to the $AlPO_4$ phase from the elemental maps of Fig. 4(d)–(f). The $AlPO_4$ does not accept Li insertion. Thus, a certain stress was applied near the boundaries between the Li-inserted grains and the $AlPO_4$ phase, and as a result,
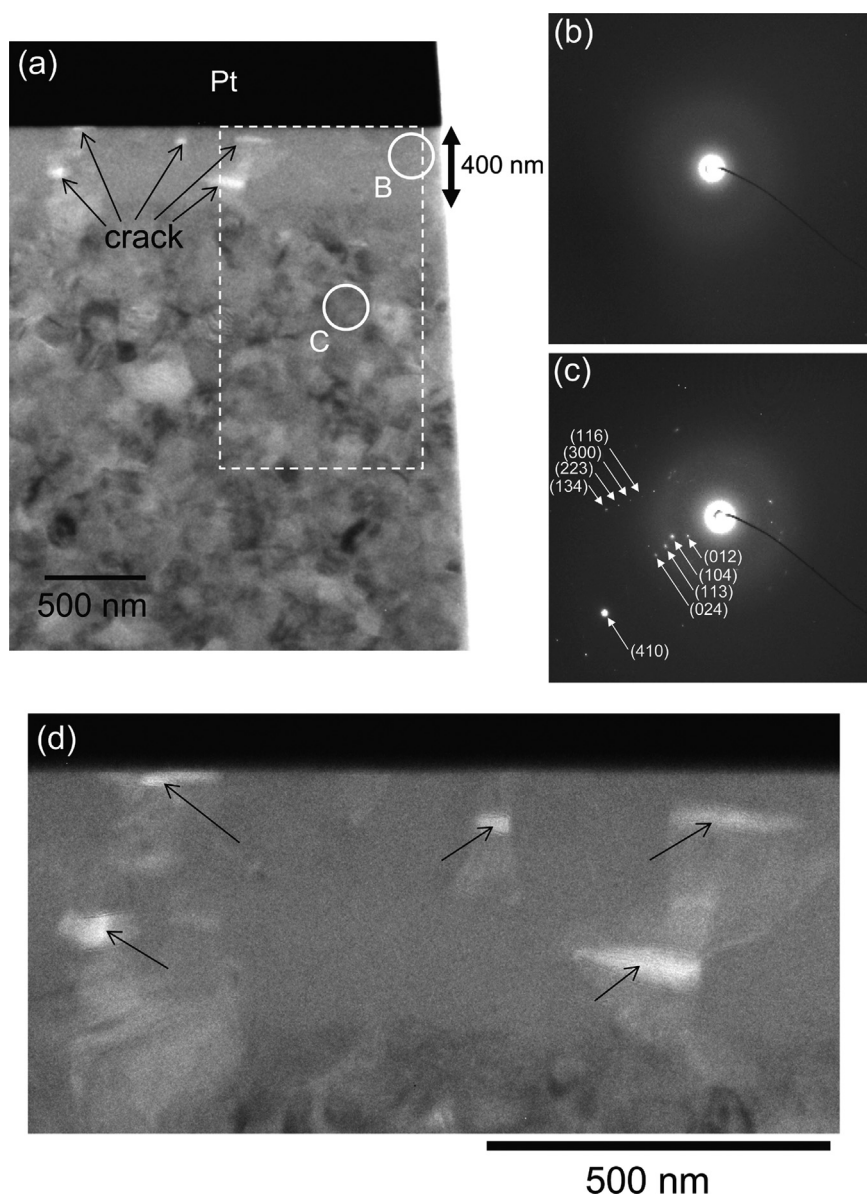
**Fig. 3.** TEM observation around the *in-situ*-formed-negative-electrode/solid-electrolyte interface. (a) TEM image around the interface. The slightly different contrast in the 400-nm width from the Pt-current-collector is the negative electrode. (b), (c) Electron diffraction patterns from the circles indicated by "B" (negative electrode region) and "C" (parent LASGTP-crystal region) in (a), respectively, showing that the Li insertion caused structural changes from a crystal to an amorphous state. (d) Enlarged image around the cracks indicated by the arrows in (a).

cracks arose around the boundaries in the negative electrode region. Those cracks were not seen in the parent LASGTP substrate. To avoid these kinds of cracks, it is necessary to prevent the formation of the $AlPO_4$ phase in the LASGTP solid electrolyte.

### 3.2. Li concentration profile detected by SR-TEM-EELS

The region surrounded by a broken line in Fig. 3(a) was selected by the rectangular slit, and the SR-TEM-EELS images around the Li-$_{K-edge}$, Ti-$_{L-edge}$, and O-$_{K-edge}$ were recorded by the CCD camera. Fig. 5(a) shows the selected TEM image, and Fig. 5(b)–(d) shows the corresponding spectrum images after subtracting the background intensity, where a power-law fitting was applied in the pre-edge background of each elemental edge and the fitted background was subtracted [20] (The Li-$_{K-edge}$ spectrum image before the background subtraction is shown in Supplementary data 2). The

intensity of each spectrum image is displayed in different colors, where a brighter color indicates higher intensity. The spectrum image size in the *y*-direction is 1880 nm in 330 pixels; thus, the size of one spectrum corresponds to 5.7 nm. The exposure time to take the images was 30 s, and sufficient signals of Li, Ti, and O elements were detected. Note that because the LASGTP glass ceramics are a mixture of amorphous and three crystalline phases, each spectrum corresponds to the integrated signals of the mixture in the *x*-direction of the selected area (Fig. 5(a)).

Fig. 6(a) shows the integrated intensity profile of Li signals along the A−B line indicated in the spectrum image of Fig. 5(b), where the average intensity in the parent LASGTP region was set to 1. This profile corresponds to the one-dimensional Li concentration distribution. The Li concentration obviously increases in the 400-nm-width region from the Pt/negative-electrode interface, where the amorphous electrode was observed in Fig. 5(a). This is clear
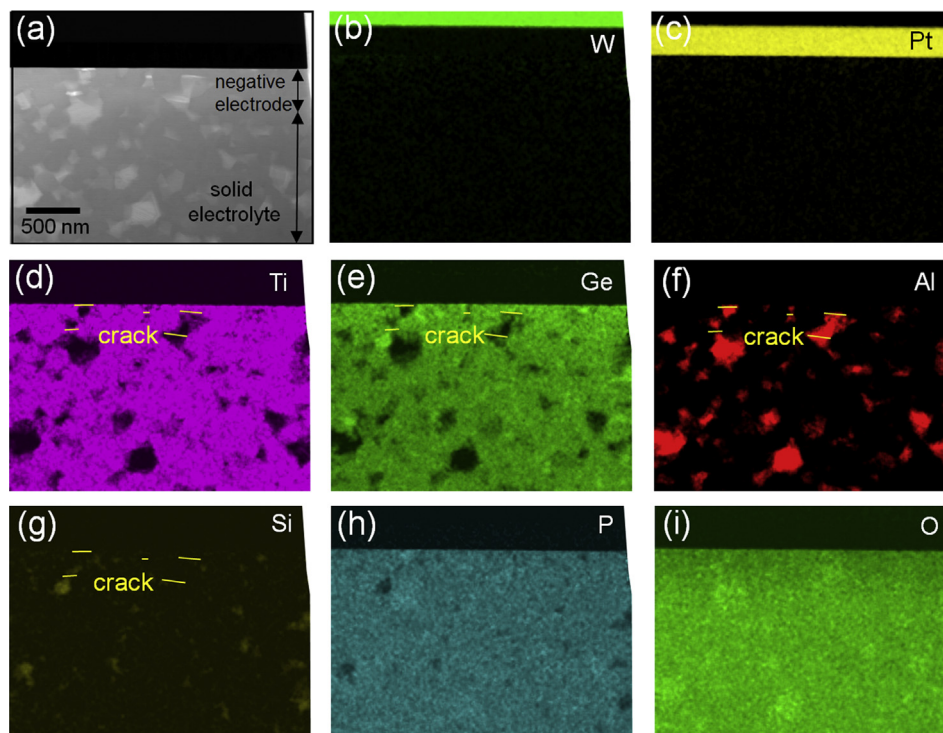
**Fig. 4.** Elemental maps around the *in-situ*-formed-negative-electrode/solid-electrolyte interface. Energy dispersive X-ray spectroscopy (EDS) was performed in a TEM to obtain the elemental distribution around the negative side region. (a) Analyzed area; (b) tungsten (W), protected layer from the focused ion beam (FIB); (c) platinum (Pt), current collector; (d) titanium (Ti); (e) germanium (Ge); (f) aluminum (Al); (g) silicon (Si); (h) phosphor (P), and (i) oxygen (O).

evidence that the Li insertion changed the structures of the parent LASGTP, and the cracks were induced by the expansion due to the inserted Li. The maximum concentration (indicated by the red arrow in Fig. 6(a)) was about 8.5 times higher than that in the parent LASGTP region, while pure crystal $LiTi_2(PO_4)_3$ materials, basic materials of the LASGTP without doping, can accept up to three times higher Li concentration, namely, $Li_3Ti_2(PO_4)_3$ [21,22]. Because the NASICON-type crystal phases changed to the amorphous phase by the Li insertion, the region probably produced many areas where the Li concentration was higher. This structural connection, that is, the gradual overlapping of the amorphous electrodes and crystal solid electrolytes, seems to result in the low interfacial resistance of Li-ion transfer.

Moreover, this Li profile that gradually increased toward the Pt/ negative-electrode interface (Fig. 6(a)) has a similar curve to the electric potential distribution we previously observed in the same battery system by EH [11,13] (see Supplementary data 3). Thus, the electrode potential in this region presumably decreases with the increase in Li concentration, and this region then works as a negative electrode.

### 3.3. Electronic structure changes of Ti and O caused by Li insertion reaction

In the spectrum image of Ti-$_{L-edge}$ (Fig. 5(c)), we can observe clear chemical shifts of the $L_2$ and $L_3$ edge lines. Fig. 6(c) shows the
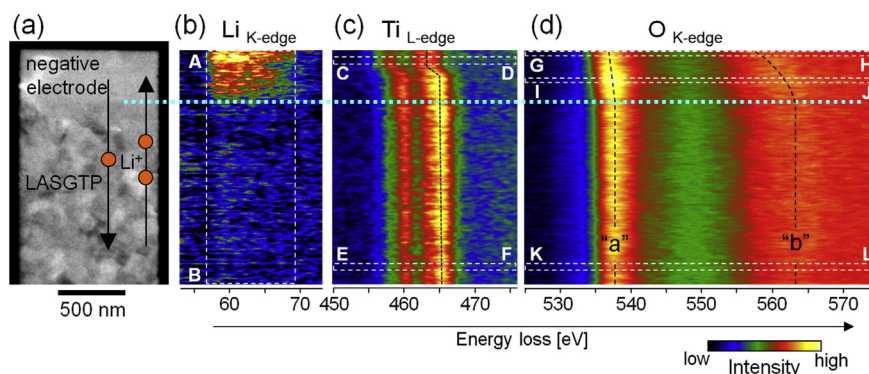


**Fig. 5.** SR-TEM-EELS images of Li-$_{K-edge}$, Ti-$_{L-edge}$, and O-$_{K-edge}$ around the *in-situ*-formed-negative-electrode/solid-electrolyte interface. A brighter color indicates higher intensity in the spectrum images. (a) TEM image selected with the rectangular slit. (b) Spectrum image of Li-$_{K-edge}$, showing higher concentration in the negative electrode. (c) Spectrum image of Ti-$_{L-edge}$. A clear chemical shift of $Ti^{4+}/Ti^{3+}$ due to the Li insertion is observable (shown by black dashed line). (d) Spectrum image of O-$_{K-edge}$. The chemical shift and spectrum intensity change of peak "a" arise from the electronic hybridization of Ti and O. The chemical shift of peak "b" shows the expansion of O−O distance of LASGTP caused by Li insertion. Both chemical shifts are guided by black dashed lines.
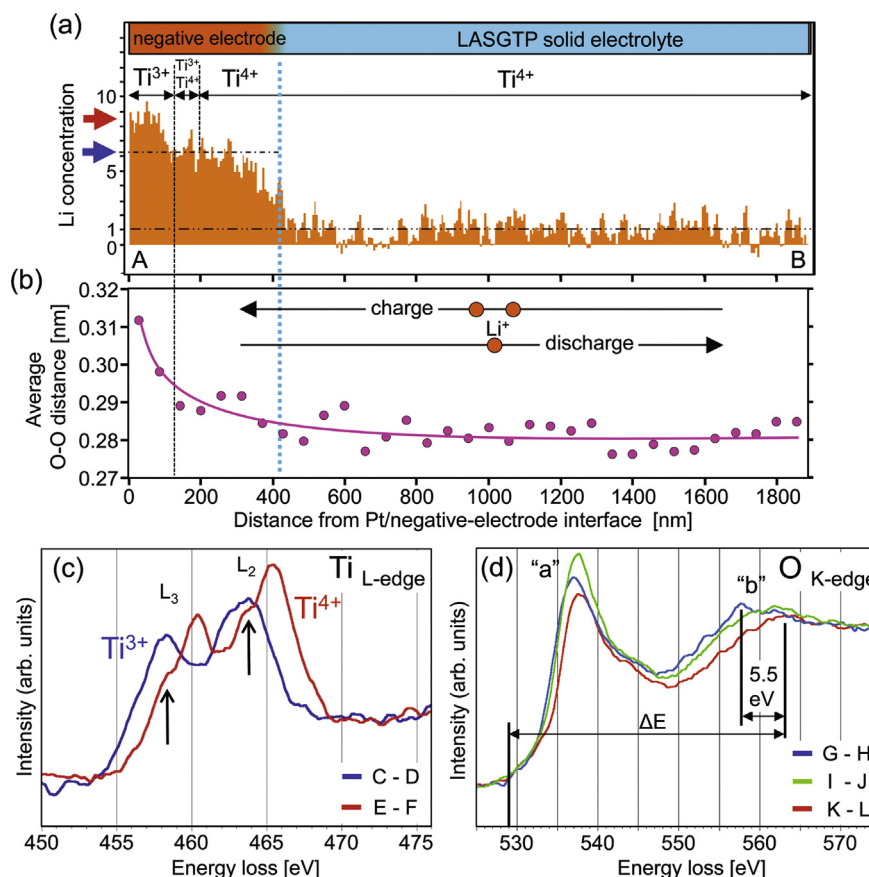
**Fig. 6.** Li concentration profile and its effects on Ti and O. (a) One-dimensional Li concentration profile along A−B in Fig. 5(b) with $Ti^{4+}$ and $Ti^{3+}$ regions. (b) Profile of average O−O distance measured by peak "b" of O spectrum image in Fig. 5(d). (c) Spectra of Ti-$_{L-edge}$ along C−D and E−F in Fig. 5(c), showing the $Ti^{3+}$ and $Ti^{4+}$ features. (d) Spectra of O-$_{K-edge}$ along G−H, I−J, and K−L in Fig. 5(d). Both peaks "a" and "b" are shifted by the Li insertion in the negative electrode.

spectra of Ti-$_{L-edge}$ along C−D (negative electrode region) and E−F (parent LASGTP region) indicated in Fig. 5(c). The spectrum in the E−F area has shoulder peaks indicated by the arrows, which is a common feature of the $Ti^{4+}$ electronic state [23,24]. The spectrum in C−D is shifted by about 1.7 eV to the direction of the lower energy-loss compared with that in E−F and does not have the clear shoulder peaks, which shows the spectrum of $Ti^{3+}$ [23,24]. It is also consistent with another study [25] that reported that the $L_2/L_3$ intensity ratio (= 1.30) of the $Ti^{4+}$ spectrum was larger than that (= 1.25) of the $Ti^{3+}$ spectrum. By using these different features of the Ti spectra, we can distinguish the $Ti^{4+}$ and $Ti^{3+}$ regions with the Li concentration profile as shown in Fig. 6(a). The changes in the Ti electronic state from $Ti^{4+}$ to $Ti^{3+}$ due to the Li insertion did not start at the negative-electrode/parent-LASGTP interface (sky blue dashed line). The boundary between the $Ti^{4+}$ and $Ti^{3+}$ regions was located about 160 nm away from the Pt/negative-electrode interface. This position is inside the negative electrode region. Moreover, the Li concentration in the $Ti^{3+}$ region is obviously higher than that in the $Ti^{4+}$ region, as shown in Figs. 5(b) and 6(a). These experimental data conclude that more than six times higher Li-concentration (indicated by the blue arrow in Fig. 6(a)) is necessary to change the electronic state of Ti in the LASGTP materials. Here, this TEM sample is in the state after the CV cycles (Fig. 1(b)). Therefore, when the sample was fully charged during the CV cycle, more Li ions were inserted, and the Li concentration in the 400-nm-wide negative-electrode region probably increased to a level higher than the level indicated by the blue arrow in Fig. 6(a). If the spectrum image of Ti were taken at the fully charged state, the boundary

of the $Ti^{4+}/Ti^{3+}$ spectrum shift could have been located around the position of the sky blue dashed line in Fig. 5(c). At the discharged state, some of the Li ions were extracted from the negative electrode region, and as a result, the electronic state of Ti changed back from $Ti^{3+}$ to $Ti^{4+}$ in the area where the Li concentration decreased to a level lower than the blue arrow level. However, the structures in the area did not recover as shown in the TEM image contrast (Fig. 5(a)). This means that the amorphous phases formed in the negative electrode lead to the smooth insertion/extraction of Li ions without large structural changes, which is why the stable cycles and low interfacial resistance are shown.

The spectrum image of O-$_{K-edge}$ in Fig. 5(d) provides a more interesting relation to the Li and Ti profiles. The image has two main "a" and "b" peaks around the energy-losses of 538 and 563 eV, respectively. We found that peak "a" started to shift slightly to a lower energy-loss at the position of the sky blue dashed line where the Li concentration increased, and also that peak "b" shifted drastically from the same position. Fig. 6(d) shows the spectra along G−H (at $Ti^{3+}$ region in the negative electrode), I−J (at $Ti^{4+}$ region in the negative electrode), and K−L (at $Ti^{4+}$ region in the parent LASGTP) indicated in Fig. 5(d). The spectrum shifts of both peaks seem to arise from the formation of the negative electrode due to the Li-insertion reaction. The "a" peaks of G−H and I−J respectively shifted by 0.9 and 0.3 eV compared with that of K−L (here, the shift values were measured after the intensity of each peak-top was normalized), and the "b" peaks also shifted by 5.5 and 1.4 eV.

Peak "a" reflects the transitions from the O 1s-core-states to 2p-states hybridized with the transition-metal Ti 3d-states [26]. Some

reports have been published about the effect of Li insertion on Ti and O electronic structures in $LiTi_2O_4$ and (Li, La) $TiO_3$ battery materials [16,17]. They proved using X-ray absorption spectroscopy and first-principles calculation that the increased number of electrons due to the electrochemically inserted Li-ions occupied the Ti and O hybridized orbit, confirming that the O-ions also contribute to the charge compensation process during the electrochemical reactions [16]. Thus, the chemical shifts of peak "a" with Li concentration were probably related to the hybridization orbit of the O 2p and Ti 3d. Furthermore, the intensity of peak "a" in I–J is higher than that in K–L, as shown in both Figs. 5(d) and 6(d). Spectrum I–J is from the $Ti^{4+}$ region in the negative electrode where some of the Li was extracted at the discharged state. Therefore, the unoccupied states increased in the hybridized orbit because of the Li extraction from the negative electrode, and the electron transitions to the O 2p states increased, resulting in the higher intensity of peak "a". In contrast, spectrum G–H is from the $Ti^{3+}$ region with sufficient Li concentration, and the unoccupied states in the hybridized orbit must be less than that of I–J. As a result, the peak intensity in G–H decreased compared with that in I–J, as shown in Figs. 5(d) and 6(d). We qualitatively interpreted the chemical shift and the intensity change of peak "a" by considering the hybridization orbit of Ti and O. However, the in-situ-formed negative electrode we presented here had disordered amorphous structures. Thus, to quantitatively explain this phenomenon on this negative electrode, first-principles calculation and EELS simulation considering the structure and composition changes would be necessary.

The chemical shifts of peak "b" show a local atomic configuration due to the Li insertion in the negative electrode. Peak "b" arises from resonance scattering of ejected core electrons between the neighboring O atoms [26,27]. The resonance effect is formulated as

$$\Delta E R^2 = constant, \tag{1}$$

where $\Delta E$ is the energy-loss position of resonance peak "b" relative to the spectrum threshold as indicated in Fig. 6(d) (we set the threshold to 529.0 eV), and $R$ is the average distance of O–O atomic pairs. This means that peak "b" is shifted in the direction of lower energy-loss when the distance of the O–O pairs increases. The results of studies of transition-metal oxides have supported Eq. (1) even if their crystal structures are different [26–28]. We derived a constant value of 2.820 (the unit of $R$ is nm) from those studies with EELS (see Supplementary data 4), and calculated the O–O distance from our experimental data in Fig. 5(d). Fig. 6(b) plots the average O–O atomic distance as a function of the distance from the Pt/negative-electrode interface. Although the O–O distance was almost constant around 0.280 nm in the parent LASGTP region, it increased to about 0.310 nm according to the Li concentration in the negative electrode region. The maximum expansion value of the O–O distance by Li insertion was about 0.030 nm (30 pm). We compared it with the average O–O distances of oxygen octahedra in pure $LiTi_2(PO_4)_3$ and $Li_3Ti_2(PO_4)_3$ crystals: 0.272 and 0.289 nm, that were derived from their atomic position data reported by Delmas's group [21,22] with 3D crystal analysis software called "VESTA" [29] (see Supplementary data 5). The expansion of the distance between the $LiTi_2(PO_4)_3$ and $Li_3Ti_2(PO_4)_3$ is 0.017 nm (17 pm). The value (30 pm) between the in-situ-formed negative electrode and parent LASGTP is much larger than the 17 pm. Therefore, in the negative electrode, the Li ions with much more than three times higher concentration were inserted into many spaces in the LASGTP glass ceramics, which is consistent with the high-density Li concentration profile measured by SR-TEM-EELS in Figs. 5(b) and 6(a).

## 4. Conclusions

We applied TEM analysis and SR-TEM-EELS to directly visualize the crystal and electronic changes caused by electrochemically inserted Li around the in-situ-formed-negative-electrode/solid-electrolyte interfaces. The highly reliable chemical shifts in the spectrum images showed the possibility that not only Ti but also O contributed to the charge compensation of the inserted Li. Furthermore, the picometer-scale expansion of the O–O distance due to the Li insertion was also visualized. The reasons the negative electrodes can be irreversibly formed in situ in the LASGTP and that explain its low interfacial resistance are the formation of amorphous phases by Li insertion and the gradual Li distribution around the interfaces. The SR-TEM-EELS technique can be used to simultaneously obtain the nanometer-scale distribution of elements and to visualize the crystal and electronic structure changes during electrochemical reactions. Therefore, this technique can potentially be applied not only to LIBs but also to fuel cell batteries, electric double-layer capacitors, and other electrochemical devices.

## Appendix A. Supplementary data

Supplementary data related to this article can be found at http://dx.doi.org/10.1016/j.jpowsour.2014.04.154.

## References

[1] M. Armand, J.-M. Tarascon, Nature 451 (2008) 652–657.
[2] J.B. Bates, N.J. Dudney, B. Neudecker, A. Ueda, C.D. Evans, Solid State Ionics 135 (2000) 33–45.
[3] B.J. Neudecker, N.J. Dudney, J.B. Bates, J. Electrochem. Soc. 147 (2000) 517–523.
[4] Y. Iriyama, T. Kako, C. Yada, T. Abe, Z. Ogumi, Solid State Ionics 176 (2005) 2371–2376.
[5] N. Ohta, K. Takada, L. Zhang, R. Ma, M. Osada, T. Sasaki, Adv. Mater. 18 (2006) 2226–2229.
[6] A. Sakuda, A. Hayashi, M. Tatsumisago, Chem. Mater. 22 (2010) 949–956.
[7] P. Birke, S. Scharner, R.A. Huggins, W. Weppner, J. Electrochem. Soc. 144 (1997) L167–L169.
[8] Y. Iriyama, C. Yada, T. Abe, Z. Ogumi, K. Kikuchi, Electrochem. Commun. 8 (2006) 1287–1291.
[9] C. Yada, Y. Iriyama, T. Abe, K. Kikuchi, Z. Ogumi, Electrochem. Commun. 11 (2009) 413–416.
[10] J. Fu, J. Am. Ceram. Soc. 80 (1997) 1901–1903.
[11] K. Yamamoto, Y. Iriyama, T. Asaka, T. Hirayama, H. Fujita, K. Nonaka, K. Miyahara, Y. Sugita, Z. Ogumi, Electrochem. Commun. 20 (2012) 113–116.
[12] K. Yamamoto, Y. Iriyama, T. Asaka, T. Hirayama, H. Fujita, C.A.J. Fisher, K. Nonaka, Y. Sugita, Z. Ogumi, Angew. Chem. Int. Ed. 49 (2010) 4414–4417.
[13] K. Yamamoto, T. Hirayama, T. Tanji, Microscopy 62 (Suppl.1) (2013) S29–S41.
[14] K. Kimoto, T. Sekiguchi, T. Aoyama, J. Electron Microsc. 46 (1997) 369–374.
[15] S. Terada, T. Aoyama, F. Yano, Y. Mitsui, J. Electron. Microsc. 51 (2002) 291–296.
[16] W. Ra, M. Nakayama, Y. Uchimoto, M. Wakihara, J. Phys. Chem. B 109 (2005) 1130–1134.
[17] M. Nakayama, T. Usui, Y. Uchimoto, M. Wakihara, M. Yamamoto, J. Phys. Chem. B 109 (2005) 4135–4143.
[18] http://www.ohara-inc.co.jp/jp/product/electronics/licgc.html.
[19] J.N. Reimers, J.R. Dahn, J. Electrochem. Soc. 139 (1992) 2091–2097.
[20] R.F. Egerton, Electron Energy-Loss Spectroscopy in the Electron Microscope, second ed., Plenum Press, New York and London, 1996, pp. 269–277.
[21] C. Delmas, A. Nadiri, J.L. Soubeyroux, Solid State Ionics 28–30 (1988) 419–423.

[22] A. Aatiq, M. Menetrier, L. Croguennec, E. Suard, C. Delmas, J. Mater. Chem. 12 (2002) 2971—2978.
[23] A. Ohtomo, D.A. Muller, J.L. Grazul, H.Y. Hwang, Nature 419 (2002) 378—380.
[24] C.C. Calvert, W.M. Rainforth, D.C. Sinclair, A.R. West, Micron 37 (2006) 412—419.
[25] E. Stoyanov, F. Langenhorst, G. Steinle-Neumann, Am. Mineral. 92 (2007) 577—586.
[26] H. Kurata, E. Lefevre, C. Colliex, R. Brydson, Phys. Rev. B 47 (1993) 13763—13768.
[27] A. Bianconi, E. Fritsch, G. Calas, J. Petiau, Phys. Rev. B 32 (1985) 4292—4295.
[28] Y. Murakami, D. Shindo, M. Kikuchi, J.-M. Zuo, J.C.H. Spence, J. Electron. Microsc. 51 (2002) 99—103.
[29] K. Momma, F. Izumi, J. Appl. Crystallogr. 44 (2011) 1272—1276.